Monthly Notices
of the
ROYAL ASTRONOMICAL SOCIETY

MNRAS **434,** 2772–2778 (2013)
Advance Access publication 2013 August 7

doi:10.1093/mnras/stt1127

RXTE and *Swift* observations of SWIFT J1729.9−3437

Ş. Şahiner,[1]⋆ S. Ç. İnam,[2] M. M. Serim[1] and A. Baykal[1]

[1]*Physics Department, Middle East Technical University, 06531 Ankara, Turkey*
[2]*Department of Electrical and Electronics Engineering, Başkent University, 06530 Ankara, Turkey*

Accepted 2013 June 18. Received 2013 May 23; in original form 2013 March 8

ABSTRACT

We analyse *Rossi X-ray Timing Explorer* (*RXTE*) and *Swift* observations of SWIFT J1729.9−3437 after its outburst from 2010 July 20 to 2010 August 12. We calculate a spin frequency and spin frequency derivative of $1.8734(8) \times 10^{-3}$ Hz and $6.42(6) \times 10^{-12}$ Hz s^{-1}, respectively from the quadratic fit of the pulse arrival times. The quadratic fit residuals fit well to a circular orbital model with a period of 15.3(2) d and a mass function of about 1.3 $M_{\odot}$, but they can also be explained by a torque noise strength of 6.8×10^{-18} Hz s^{-2}. Pulse profiles switch from double peaked to single peaked as the source flux continues to decrease. We find that the pulse shape generally shows no strong energy dependence. The hardness ratios reveal that the source becomes softer with decreasing flux. We construct a single spectrum from all the available *RXTE* and *Swift* observations. We find that adding an *Fe* line complex feature around 6.51 keV slightly improves the spectral fit. We also find that *Fe* line flux correlates with X-ray flux which might indicate the origin of the *Fe* emission as the source itself rather than the Galactic ridge.

Key words: accretion, accretion discs – stars: neutron – pulsars: individual: SWIFT J1729.9−3437 – X-rays: binaries.

1 INTRODUCTION

SWIFT J1729.9−3437 is a transient X-ray pulsar discovered during all-sky monitoring with the *Swift* Burst Alert Telescope (BAT) on 2010 July 13 (Markwardt, Krimm & Swank 2010a). At the same time, *Rossi X-ray Timing Explorer* (*RXTE*) Proportional Counter Array (PCA) monitoring scans of the Galactic centre region confirmed a gradual increase in flux from a position consistent with the *Swift* position of the source (RA = 262.537 46, Dec. = −34.612 39). Consecutive *RXTE*−PCA pointings identified SWIFT J1729.9−3437 as a pulsar with ∼530 s pulsations (Markwardt, Krimm & Swank 2010b). Markwardt et al. (2010b) also suggested that the X-ray spectrum of the source is compatible with basic X-ray pulsar spectra, modelled by an absorbed power law with a high-energy cut-off.

In this paper, we analyse *RXTE* and *Swift* observations of SWIFT J1729.9−3437 and examine the spectral and timing properties of its outburst from 2010 July 20 to 2010 August 12 (MJD 553 97−554 20). In Section 2, we describe the observations that we analyse. In Sections 3 and 4, we present our timing and spectral analysis results. In Section 5, we discuss our results and conclude.

⋆E-mail: seyda@astroa.physics.metu.edu.tr (ŞŞ); inam@baskent.edu.tr (SÇİ); altan@astroa.physics.metu.edu.tr (AB); muhammed@astroa.physics.metu.edu.tr (MMS)

2 OBSERVATIONS

2.1 *RXTE*

11 pointing *RXTE*−PCA observations of SWIFT J1729.9−3437 were performed between 2010 July 20 and 2010 August 8. The total exposure time is about 42 ks. PCA consisted of five co-aligned identical proportional counter units (PCUs) (Jahoda et al. 1996) each having an effective area of approximately 1300 cm^2. The energy range of PCA was from 2 to 60 keV, with an energy resolution of 18 per cent at 6 keV. The field of view (FOV) at full width at half-maximum was about 1°. Generally, various PCUs were turned off during PCA observations. The responses of PCU0 and PCU1 were not well known due to loss of their propane layers. Furthermore, the responses of the top anode layers were modelled better than the other layers. Although the number of active PCUs during the observations of SWIFT J1729.9−3437 varied between one and three, we select only data from the top anode layer of PCU2 because of the reasons mentioned above.

The standard software tools of 'HEASOFT V.6.11' are used for the PCA data analysis. Data is filtered by selecting times when the elevation angle is greater than 10°, the offset from the source is less than 0.02 and the electron contamination of PCU2 is less than 0.1. The background extraction for spectra and light curves are done by using the latest PCA background estimator models supplied by the *RXTE* Guest Observer Facility, 'EPOCH 5C'.

© 2013 The Authors
Published by Oxford University Press on behalf of the Royal Astronomical Society

Downloaded from https://academic.oup.com/mnras/article-abstract/434/4/2772/954751 by MIDDLE EAST TECHNICAL UNIVERSITY LIBRARY user on 24 July 2020

During the extraction of spectra, Standard2f mode data is considered with 128 energy channels and 16 s time resolution. Relevant response matrices for spectra are created by 'PCARSP V.11.7.1'. Furthermore, we construct pulse phase resolved spectra with the tool 'FASEBIN REV.1.8' by using Good Xenon mode event data and 125 μs time resolution event files (E_125us_64M_0_1s") when Good Xenon mode data is not available. From these spectra, we generate energy-resolved pulse profiles by obtaining the count rates per phase bin with the tool 'FBSSUM'. The 1 s binned 3–20 keV light curves are produced from Good Xenon and E_125us_64M_0_1s" events.

2.2 *SWIFT*

After the discovery of SWIFT J1729.9−3437 by the *Swift*−BAT (Barthelmy et al. 2005) all-sky monitoring on 2010 July 13 (Markwardt et al. 2010a), a total of 11 follow-up X-ray Telescope (XRT; Burrows et al. 2005) observations (each ∼3 ks) were carried out between 2010 July 20 and 2010 August 12. XRT is a focusing instrument on board the *Swift* satellite (Gehrels et al. 2004) which operates between 0.2 and 10 keV energy range. XRT has an effective area of 110 cm^2 at 1.5 keV with a spatial resolution of 18 arcsec and the FOV of 23.6 arcmin × 23.6 arcmin. Operation mode of XRT switches between photon counting (PC), imaging and timing depending on the brightness of the observed source. Pointing observations of SWIFT J1729.9−3437 are in the PC mode. Screened event files are produced by the 'XRTDAS V.2.7.0' standard data pipeline package 'XRTPIPELINE V.0.12.6'. Standard grade filtering (0–12) is applied to PC mode.

The spectral extraction is carried out by filtering appropriate regions using 'XSELECT V.2.4B'. For the observations in which the XRT count rate is high enough (above 0.5 cts s^{-1}) to produce event pile-up, source region is selected to be annular. We compared the observed and nominal point spread function (PSF) (Vaughan et al. 2006) and decided the size of the core affected in order to determine the radius of the inner circle of the annulus. For this purpose, we first modelled the outer wings (>15 arcsec) of the PSF with a King function which has typical parameter values for XRT (Moretti et al. 2005). Then the model is extrapolated to the inner region for comparison with the observed PSF and the size of the piled-up region is determined from the deviation point between the data and the model. For the brightest observations an exclusion region of radius ∼9 arcsec is sufficient to correct pile-up. For low count rate observations a circular region of radius 47 arcsec is selected for the source spectral extraction. Source regions are centred on the position determined with 'XRTCENTROID V.0.2.9'. A circular source-free region with 140 arcsec radius is selected for the background spectral extraction. Resulting spectral files are grouped to require at least 50 counts per bin using the ftool 'GRPPHA V.3.0.1', for the χ^2 statistics to be applicable. We used the latest response matrix file (version v013) and created individual ancillary response files using the tool 'XRTMKARF V.0.5.9' with the exposure map produced by 'XRTEXPOMAP V.0.2.7'. Spectral analysis is performed using 'XSPEC V.12.7.0'.

For the timing analysis, arrival times of XRT events are first corrected to the Solar system barycenter by using the tool 'BARYCORR V.1.11'. Then, background-subtracted XRT light curves in the 0.2–10 keV energy range, corrected for pile-up, PSF losses and vignetting, are extracted by using the highest possible time resolution (2.51 s) for PC mode data.

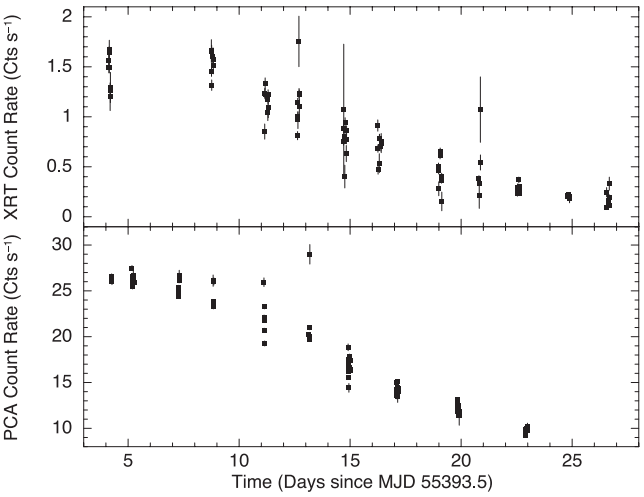


Figure 1. 530 s binned light curves from *Swift*−XRT (0.3–10 keV; upper panel) and *RXTE*−PCA (3–20 keV, PCU2 top layer; lower panel) observations.

3 TIMING ANALYSIS

3.1 Timing solution

For the timing analysis, we use 1 s binned *RXTE*−PCA and 2.51 s binned *Swift*−XRT light curves of the source. To illustrate the temporal variation of the pulse phase averaged count rate of the source, in Fig. 1, we present 530 s binned versions of these light curves. These background-subtracted light curves are also corrected to the barycenter of the Solar system.

In order to estimate pulse periods of the source, the *RXTE*−PCA time series is folded on statistically independent trial periods (Leahy et al. 1983). Template pulse profiles are formed from these observations by folding the data on the period giving maximum χ^2. Then the barycentred *Swift*−XRT time series are also folded over the best period obtained from *RXTE*. Pulse profiles consisting of 20 phase bins are represented by their Fourier harmonics (Deeter & Boynton 1985). Using cross-correlation of pulses between template and in each observation, we obtain the pulse arrival times.

We are able to connect all the pulse arrival times of the observations in phase over the whole observation time span. Following the approach of Deeter, Boynton & Pravdo (1981), we find that it is possible to fit the pulse arrival times to the second-order polynomial

$$\delta\phi = \delta\phi_o + \delta\nu(t - t_o) + \frac{1}{2}\dot{\nu}(t - t_o)^2, \quad (1)$$

where $\delta\phi$ is the pulse phase offset found from the pulse timing analysis, t_o is the epoch for folding; $\delta\phi_o$ is the residual phase offset at t_o; $\delta\nu$ is the correction to the pulse frequency at time t_0; $\dot{\nu}$, being the pulse frequency derivative, is the second derivative of the pulse phase. In Fig. 2, we present the pulse phases and the residuals of this quadratic fit.

In Fig. 3, we show typical *Swift*−XRT and *RXTE*−PCA pulse profiles. As seen from this figure, the *Swift* pulse has larger error bars and less signal-to-noise ratio relative to the *RXTE* pulse. In the pulse timing analysis, we find that the error bars of the pulse phases of *RXTE* and *Swift* are inversely correlated with the signal-to-noise ratio of the pulses of each observation.

The residuals shown in Fig. 2 fit well to a sinusoidal function with a period of 15.3(2) d. This corresponds to a circular orbital model, parameters of which are listed in Table 1. This circular model has a

Downloaded from https://academic.oup.com/mnras/article-abstract/434/4/2772/954751 by MIDDLE EAST TECHNICAL UNIVERSITY LIBRARY user on 24 July 2020

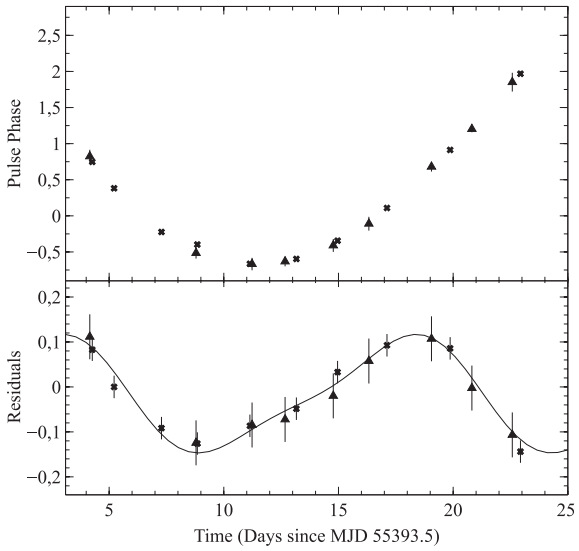


Figure 2. Pulse phases and their residuals after a quadratic fit. Crosses and triangles represent data from *RXTE*−PCA and *Swift*−XRT, respectively. The solid line in the bottom panel corresponds to the elliptical orbital model with an upper limit of eccentricity of 0.60 and $T_{\pi/2} = 5^{\circ}$ and circular orbital parameters listed in Table 1.

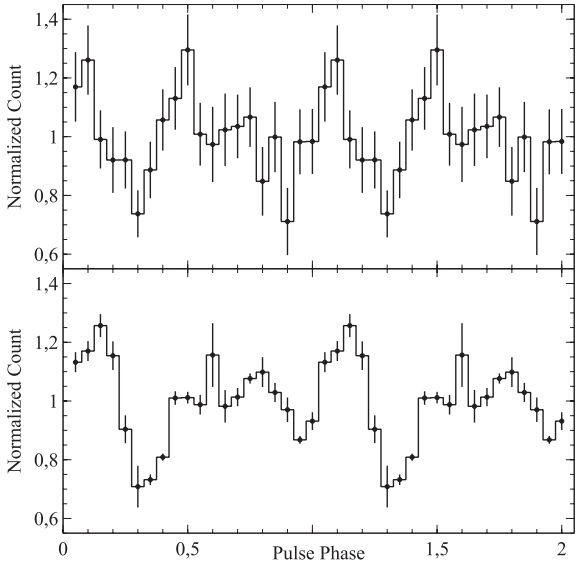


Figure 3. Two pulse examples obtained from the *Swift*−XRT observation at MJD 553 97.66 (top panel) and the *RXTE*−PCA observation at MJD 553 97.77 (bottom panel).

Table 1. Timing solution and orbital model of SWIFT J1729.9−3437.

Timing solution parameter	Value
Timing epoch (MJD)	553 93.50(6)
Frequency (Hz)	$1.8734(8) \times 10^{-3}$
Frequency derivative (Hz s^{-1})	$6.42(6) \times 10^{-12}$
Circular orbital model parameter	Value
Orbital epoch (MJD)	553 95.7(6)
$\frac{a}{c} \sin i$ (lt s)	65(3)
Orbital period (d)	15.3(2)

reduced χ^2 of 1.0. Using an elliptical model we find an upper limit for the eccentricity as 0.6 (see bottom panel of Fig. 2). In this case, reduced χ^2 is found to be 0.4. This small reduced χ^2 value indicates that the elliptical orbital model 'overfits' data.

The residuals of the quadratic can alternatively express the noise process due to random torque fluctuations (Bildsten et al. 1997; Baykal et al. 2007). In order to estimate the noise strength, we fit a cubic polynomial to the residuals of the pulse arrival times. The observed time series is simulated by the Monte Carlo technique for a unit white noise strength defined as $P_{\dot{\nu}}(f) = 1$ and fitted to a cubic polynomial in time. Then the square of the third-order polynomial term is divided into the value from Monte Carlo simulations (Deeter 1984; Cordes 1980). The torque noise strength is obtained as 6.8×10^{-18} Hz s^{-2}. This value of noise strength estimate is comparable with those of other accretion powered sources such as wind accretors e.g. Vela X−1, 4U 1538−52 and GX 301−2 which has the values changing between 10^{-20} and 10^{-18} Hz s^{-2} (Bildsten et al. 1997). Her X−1 and 4U 1626−67, which are disc accretors with low-mass companions, have shown pulse frequency derivatives consistent with noise strengths 10^{-21} to 10^{-18} Hz s^{-2} (Bildsten et al. 1997). Therefore, residuals of quadratic fit can also be associated with torque noise fluctuation of the source.

3.2 Pulse profiles and hardness ratios

A double-peaked pulse profile is observed in the first five *RXTE*−PCA observations of SWIFT J1729.9−3437 (see panel (A) of Fig. 4); however, one peak loses its intensity starting from the middle of the observation on MJD 554 06.7 (see panel (B) Fig. 4) as the source flux continues to decrease after the burst. The peak value of 2–10 keV unabsorbed flux is 3.04×10^{-10} erg cm^{-2} s^{-1} on MJD 553 98.7, during its gradual decrease it reaches 1.96×10^{-10} erg cm^{-2} s^{-1} on MJD 554 08.5, when the shape of the pulse profile changes (see panel (C) Fig. 4). The minimum flux observed for the last *RXTE*−PCA observation on MJD 554 16.4 is 1.36×10^{-10} erg cm^{-2} s^{-1}. These flux values

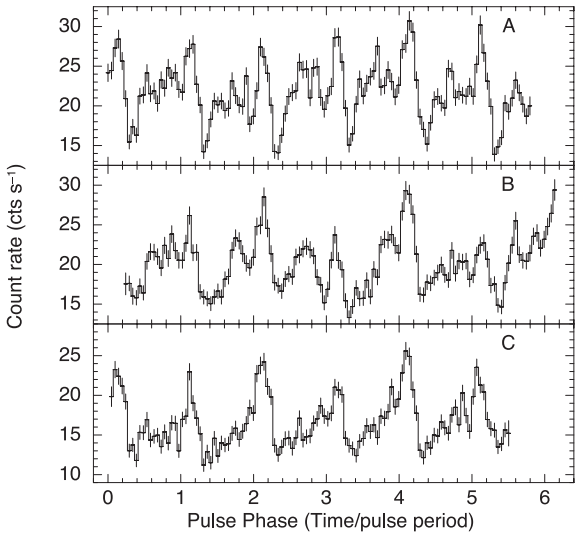


Figure 4. 26 s binned light curves of three different *RXTE*−PCA observations (3−20 keV, PCU2 top layer). Time values are converted to phases (or time/pulse period) for arbitrary observation epochs. The IDs and mid-times of the observations are (A) 95044-05-02-02 at MJD 554 04.6, (B) 95044-05-02-03 at MJD 554 06.7, (C) 95044-05-03-00 at MJD 554 08.5.

Downloaded from https://academic.oup.com/mnras/article-abstract/434/4/2772/954751 by MIDDLE EAST TECHNICAL UNIVERSITY LIBRARY user on 24 July 2020

are calculated from the model flux of individual spectral fitting of each observation.

To search for a possible energy dependence of the pulse shape change, we construct pulse profiles in five energy bands, i.e. 3–8, 8–13, 13–18, 18–25 and 25–60 keV. Two examples for the energy-resolved pulse profiles, one for double peaked and one for single peaked, are given in Fig. 5. We find that 8–13 keV and 13–18 keV pulses are stronger (they have higher pulse fraction) than the 3–8 keV and 18–25 keV pulses in all observations. In 25–60 keV, the pulse fraction noticeably drops. The pulse shape shows no strong energy dependence except for the two observations on MJD 554 00.78 (ID:95044-05-02-00 see Fig. 5) and MJD 554 04.63 (ID:95044-05-02-02). In these two exceptions, the secondary peak around pulse phase 0.3 loses its intensity at the 18–25 keV energy band.

We construct hardness ratio plots from the energy-resolved light curves. Daily averaged count rates from 3–8, 8–13, 13–18 and 18–25 keV light curves are used to plot hardness ratios HR1: 8–13 keV/3–8 keV and HR2: 18–25 keV/13–18 keV over time (see left-hand panels of Fig. 6). HR1 shows a noticeable evolution with respect to time, it remains almost constant at a value ∼1.1 until MJD 554 06.7 and a gradual decrease starts after the sixth observation. The interval with constant HR1 corresponds to times when the pulse profile is double peaked, whereas the decreasing interval of HR1 coincides with the times when the pulse profile is single peaked. Nevertheless, it should be noted that the pulse profiles show no significant variation in the corresponding energy bands (see Fig. 5). Furthermore, 530 s binned hardness ratios are plotted over the total count rate in 3–25 keV band (see right-hand panels of Fig. 6). A

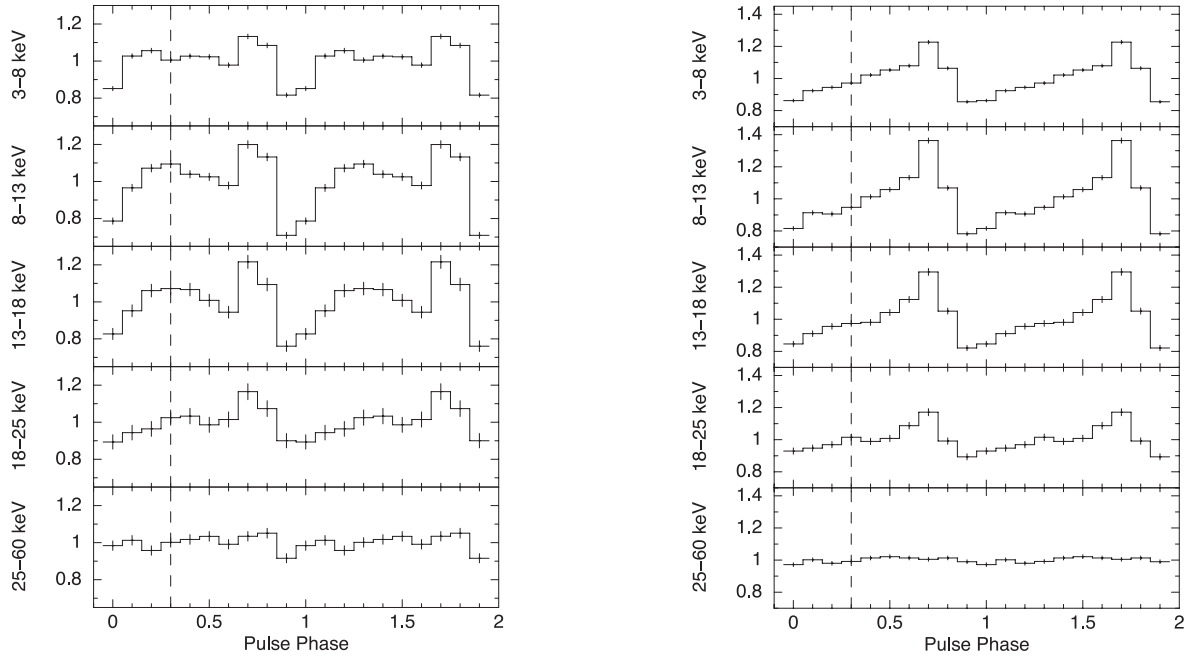


Figure 5. Energy-resolved pulse profiles of *RXTE*−PCA observations on MJD 554 00.78 (left; ID:95044-05-02-00) and MJD 554 08.46 (right; ID:95044-05-03-00). The unit of *y*-axis of each plot is normalized count from the specified energy interval. The dashed line represents the mid-point of the secondary peak.

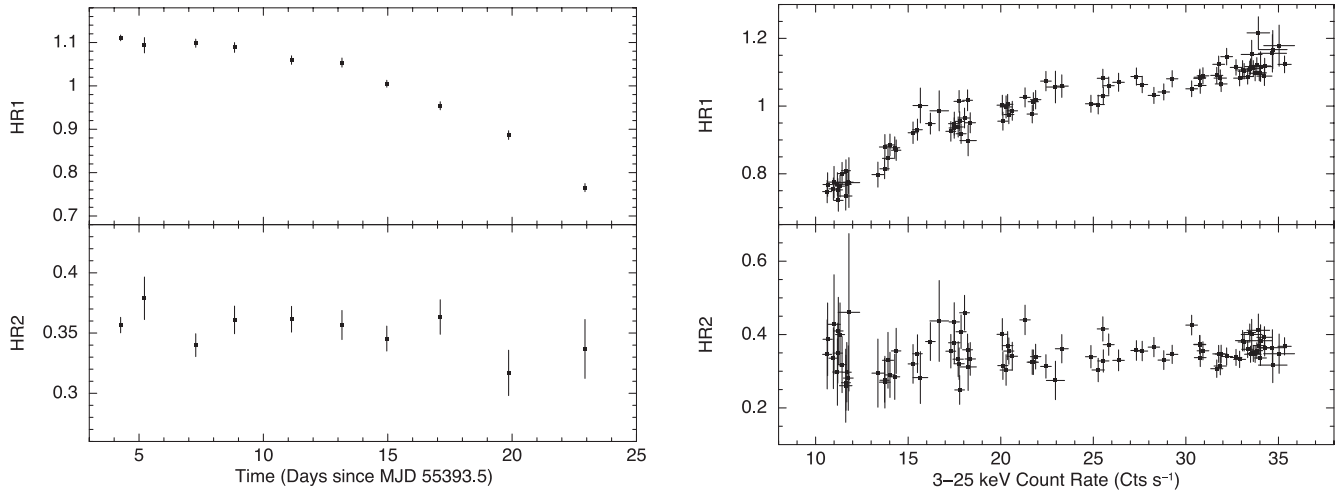


Figure 6. Hardness ratios of energy-resolved light curves. Daily averaged time evolutions are plotted on the left, whereas 530 s binned hardness ratios over 3–25 keV PCU2 count rates are plotted on the right. Specified abbreviations on *y*-axis of each panel stand for HR1: 8–13 keV/3–8 keV, HR2: 18–25 keV/13–18 keV.

Downloaded from https://academic.oup.com/mnras/article-abstract/434/4/2772/954751 by MIDDLE EAST TECHNICAL UNIVERSITY LIBRARY user on 24 July 2020

noticeable correlation is again observed for HR1. As the source flux decreases during the ongoing decline of the outburst, the emitted radiation becomes softer.

4 SPECTRAL ANALYSIS

4.1 Overall spectrum

A preliminary spectral analysis for the first pointed observations of SWIFT J1729.9−3437 was performed by Markwardt et al. (2010b). In this paper, we extend the spectral study by using all the available observations of the source defined in Section 2. Basically, the spectra can be modelled by a power law with a high-energy cut-off and photoelectric absorption as it is suggested by Markwardt et al. (2010b). Among the several models that describe the cut-off power law, the best fit is achieved by 'CUTOFFPL' model in 'XSPEC'. An additional Gaussian component is also required for a weak *Fe* emission line around 6.4 keV. During the simultaneous fitting of *Swift*−XRT and *RXTE*−PCA spectra we included a multiplicative constant factor in the model to account for the normalization uncertainty between the two instruments. The data and its best fit are plotted in Fig. 7 and the corresponding spectral parameters are given in Table 2.

The energy ranges for the simultaneous spectral analysis are initially selected to be 0.3–9.3 keV for the XRT spectrum and 3–25 keV for the PCA spectrum. Individually these spectra have similar shapes that can be modelled with the same models, apart from an offset in absolute flux calibration. However individual modelling of the data from different instruments yields different absorption parameters due to different instrumental band passes (Markwardt et al. 2010b). During the simultaneous fitting trials, we observe large residuals for the first energy bins of the PCA spectrum although the fit is adequate for the XRT spectrum. Therefore, we exclude energies below 5 keV for the PCA spectrum, since the XRT spectrum has more spectral energy bins in soft X-rays.

The FOV of PCA is large and SWIFT J1729.9−3437 is near the Galactic ridge. The thermal emission from the ridge is usually known to contaminate the spectral count rates of the source. During the analysis of the first PCA observation, the weak line at ∼6.6 keV reported by Markwardt et al. (2010b) was suggested to be a contamination, since it could not be resolved in the spectrum of the first XRT observation. We tried to handle this issue in overall PCA spectrum with fixed additive Galactic ridge models. We confirm that the flux of the source is two orders of magnitude bigger than the flux of the Galactic ridge (Valinia & Marshall 1998) therefore, we conclude that the contamination could be small enough to be neglected. Furthermore; addition of the Gaussian model component for the *Fe* line improves the individual fit of the 0.3–9.3 keV XRT spectrum after combining data from all XRT observations by reducing the reduced χ^2 from 1.08 (χ^2/d.o.f. = 159.0/147) to 0.98 (χ^2/d.o.f. = 143.8/146). The F-test probability that this improvement is achieved just by chance is 1.3×10^{-4}. Therefore, we suggest that the *Fe* emission originates from SWIFT J1729.9−3437. The line energy found for the source is shifted from the neutral value of *Fe* Kα (∼6.4 keV), which may be a consequence of an excess of ionization.

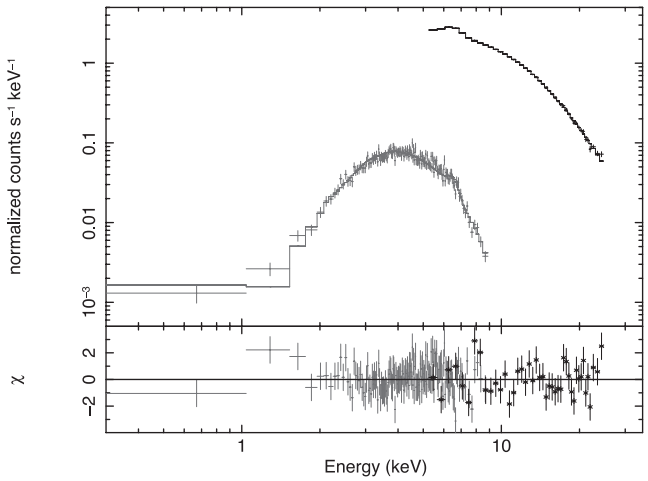


Figure 7. Simultaneous spectral fitting of *Swift*−XRT (0.3–9.3 keV; grey) and *RXTE*−PCA (5–25 keV; black) data. The data and its best fit with WABS×(CUTOFFPL+GAU) ($\chi^2 = 1.09$; solid line) are shown in upper panel, the residuals are given in the lower panel.

Table 2. Best-fitting (WABS×(CUTOFFPL+GAU)) spectral parameters for the simultaneous fitting of *Swift*−XRT and *RXTE*−PCA data shown in Fig. 7. C_1 and C_2 are the multiplicative constant factors for different instruments. All uncertainties are calculated at the 90 per cent confidence level.

Parameter		Value
C_1	for XRT	1.00 (fixed)
C_2	for PCA	$1.55^{+0.04}_{-0.04}$
$n_{\rm H}$	(10^{22} cm^{-2})	$8.27^{+0.37}_{-0.36}$
Γ		$1.23^{+0.07}_{-0.07}$
Γ Norm.	(10^{-2} cts cm^{-2} s^{-1})	$2.42^{+0.26}_{-0.25}$
$E_{\rm fold}$	(keV)	$16.50^{+1.79}_{-1.52}$
$E_{\rm Fe}$	(keV)	$6.51^{+0.03}_{-0.03}$
$\sigma_{\rm Fe}$	(keV)	$0.25^{+0.06}_{-0.05}$
Fe Norm.	(10^{-4} cts cm^{-2} s^{-1})	$4.68^{+0.49}_{-0.41}$
Unabs. $F_{0.3-9.3\,\rm keV}$	(10^{-10} erg cm^{-2} s^{-1})	$2.08^{+0.017}_{-0.024}$
Unabs. $F_{5-25\,\rm keV}$	(10^{-10} erg cm^{-2} s^{-1})	$3.00^{+0.004}_{-0.016}$
Reduced χ^2 (d.o.f.)		1.09 (187)

In accretion powered pulsars, the *Fe* Kα line is produced by the reprocessing of the hard X-ray emission in the relatively low ionized and cool matter surrounding the pulsar. The correlation of the iron line intensity and the continuum intensity in many sources (e.g. Vela X−1: Ohashi et al. 1984, GX 301−2: Leahy et al. 1989) is specified to be the evidence for the fluorescence of X-ray continuum by the cold material. As the continuum intensity increases the illumination of the matter increases and the line intensity strengthens. We measure *Fe* line flux values from the individual *RXTE* observations of SWIFT J1729.9−3437 by using the 'CFLUX' model in 'XSPEC' and find that they correlate with the source flux values (see Fig. 8). In Fig. 8, the dotted line represents the linear fits to the data, with a slope of 0.46 ± 0.12. The Pearson product–moment correlation coefficient between *Fe* line flux and unabsorbed source flux at 2–10 keV is 0.96. The null-hypothesis probability calculated from the Student's t-distribution (two-tailed) is 1.2×10^{-5}. This correlation also confirms the origin of the *Fe* emission.

4.2 Pulse phase resolved spectra

We construct pulse phase resolved spectra of SWIFT J1729.9−3437 from the first three *RXTE*−PCA observations. There are two motivations to the data selection. First, the brightest of the observations are selected to ensure the best signal-to-noise ratio possible.

Downloaded from https://academic.oup.com/mnras/article-abstract/434/4/2772/954751 by MIDDLE EAST TECHNICAL UNIVERSITY LIBRARY user on 24 July 2020

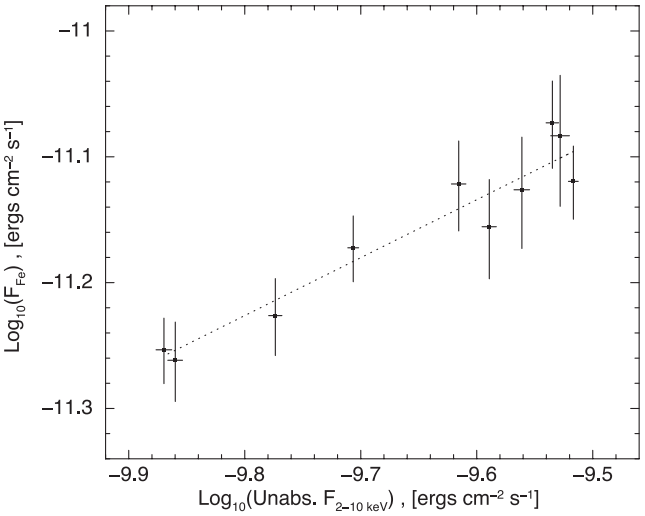


Figure 8. Variation of *Fe* line flux with the X-ray flux from *RXTE*−PCA observations. The error bars indicate uncertainties at 1σ (68 per cent) confidence level. The dotted line represents the linear fits to the data.

Secondly, the selected observations are the only ones that have 256 channels Good Xenon event mode data available, which is required for the 'FASEBIN' tool. The timing solution found for the source in Section 3.1 is appended to the timing files of the 'FASEBIN' tool for correct phase-binning. The pulse period is divided into five equal segments resulting in ∼2.1 ks exposure time for each phase bin spectrum.

We model 3–25 keV spectra with the same models used for the overall spectrum in the previous section. As we do not observe any significant change in the hydrogen column density ($n_{\rm H}$) and the *Fe* line energy during the preliminary fitting trials, we fixed these parameters during the analysis in order to better constrain the other parameters of the fits. The photon index and the folding energy of the high-energy cut-off ($E_{\rm fold}$) are found to be varying within pulse phases (see Fig. 9). The phase dependence of photon index is in anticorrelation with the pulsed flux. The Pearson product–moment correlation coefficient between pulsed flux and photon index values is −0.87 and the corresponding null-hypothesis probability (two-tailed) is 0.06. The null-hypothesis probability of this anticorrelation is quite significant but our results still indicate that the softest emission is observed at the unpulsed phase around 0.05; from which we might suggest a possible physical relation between the parameters. The $E_{\rm fold}$ values show a similar trend as the photon index values, which means softer spectra have higher cut-off energies. The Pearson product–moment correlation coefficient between $E_{\rm fold}$ and photon index values is 0.96 and the corresponding null-hypothesis probability (two-tailed) is 0.01. Although the correlation analysis indicates a strong dependence between the parameters, one should note that the uncertainties in the parameters are not taken into account during this analysis. When the large uncertainties in $E_{\rm fold}$ values are taken into account the data is consistent with a constant value of ∼11.7 keV. Therefore, it is difficult to infer a clear variation of the $E_{\rm fold}$ with the pulse phase, suggesting a rather marginal detection.

5 SUMMARY AND DISCUSSION

In this paper, we study timing and spectral properties of SWIFT J1729.9−3437 using *RXTE* and *Swift* observations of its outburst from 2010 July 20 through 2010 August 12 (MJD 553 97–554 20).

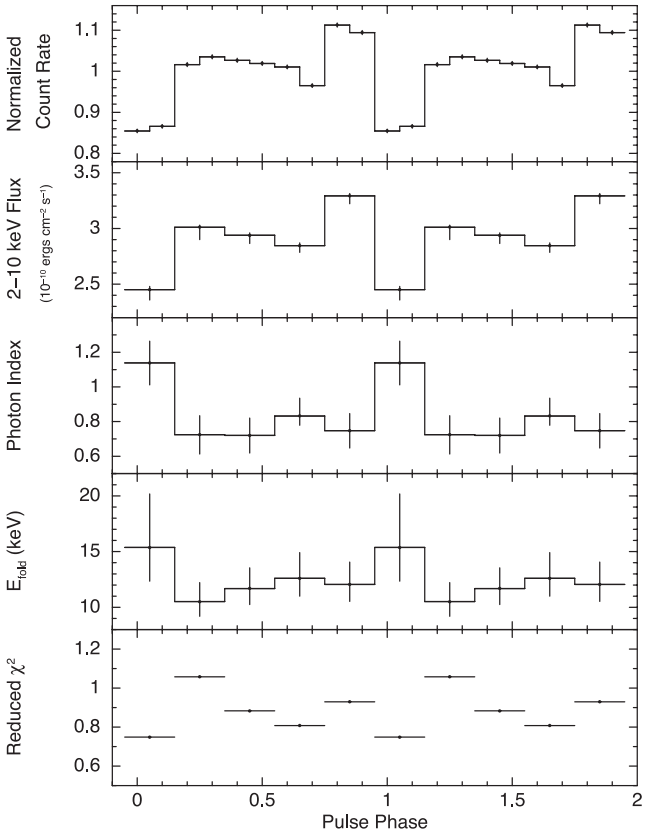


Figure 9. Pulse phase resolved variations of the spectral parameters with 5 phase bins for the first three *RXTE*−PCA observations. The pulse profile is plotted in 10 phase bins at the top panel. From top to bottom, we show the pulse profile, 2–10 keV unabsorbed flux, the photon index, the folding energy of exponential roll-off and reduced χ^2 of the fits. All uncertainties are calculated at the 90 per cent confidence level. For clarity, the data points are repeated for a cycle.

From these observations with a time span of ≃23 d, we find that arrival times can be fit to a quadratic. From this fit, we calculate a spin frequency and spin frequency derivative of $1.8734(8) \times 10^{-3}$ Hz and $6.42(6) \times 10^{-12}$ Hz s^{-1}, respectively. The residuals of the quadratic is further found to fit a circular orbital model with $\frac{a}{c} \sin i = 65(3)$ lt s and an orbital period of 15.3(2) d. We also try an elliptical model and find an upper limit for eccentricity as 0.60. However, this model overfits the data with a reduced χ^2 of 0.40. Future observations might help to refine orbital parameters of the source.

Using this $\frac{a}{c} \sin i$ value, we find the mass function ($\frac{4\pi^2}{G} \frac{(a \sin i)^3}{P^2_{\rm orbital}}$) to be about 1.3 $M_\odot$. An orbital period of 15.3 d and a spin period of 533.76 s puts the source in line with the accretion powered pulsars with supergiant companions, in the Corbet diagram (Corbet 1984; Drave et al. 2012). On the other hand, the small mass function obtained from the circular orbital model should be an indication of a small orbital inclination angle. If the circular orbital model is preferred as the model fitting the residuals of the quadratic fit, this indicates that we observe the binary system nearly edge-on.

Alternatively, the residuals of the quadratic fit can be explained by a torque noise strength of 6.8×10^{-18} Hz s^{-2}. This value is quite consistent with other accreting X-ray binaries (Baykal & Ögelman 1993; Bildsten et al. 1997). Future observations are needed to understand the exact nature of the source.

Initially, a double-peaked pulse profile is observed in the light curves of the source. Then, we find that one peak loses its intensity

Downloaded from https://academic.oup.com/mnras/article-abstract/434/4/2772/954751 by MIDDLE EAST TECHNICAL UNIVERSITY LIBRARY user on 24 July 2020

starting from the middle of the observation on MJD 554 06.7 as the source flux continues to decrease after the burst. To study the energy dependence and temporal variability of the pulse profiles, we construct pulse profiles with five different energy bands shown in Fig. 5. We observe stronger pulses in the 8–13 keV and 13–18 keV energy bands but generally the pulse shape shows no strong energy dependence. Double to single peak transition seen in this source might be due to a sharp decline in the intensity of the radiation coming from the fan beam, since the formation of fan beam strongly depends on the luminosity of the source as for EXO 2030+375 (Parmar, White & Stella 1989) and GX 1+4 (Paul et al. 1997). However, lack of significant energy dependence of the pulse profiles makes the fan beam explanation implausible since fan beams are expected to be spectrally harder than pencil beams.

In order to have a basic understanding of spectral variability of the whole observations, we study hardness ratios of the source. From the hardness ratio plots (see Fig. 6), we suggest that the emitted radiation becomes softer as the source flux decreases during the ongoing decline of the outburst. The similar spectral softening with decreasing flux was reported before for 1A 0535+262, A 1118−616, SWIFT J1626.6−5156, XTE J0658−073 and GRO J1008−57 using hardness–intensity relations (Reig & Nespoli, 2013).

To extend the preliminary spectral analysis of Markwardt et al. (2010b), we also construct a single spectrum from all the available *RXTE* and *Swift* observations (see Fig. 7 and Table 2). We find that adding an *Fe* line complex feature with a peak at 6.51 keV slightly improves the spectral fit. We discuss that this *Fe* line feature is more likely originated from the source as the Galactic ridge emission is too weak to explain this emission alone. We also measure *Fe* line flux values from the individual *RXTE* observations of the source and find that they correlate with the source flux values (see Fig. 8). This correlation confirms the origin of the *Fe* emission as the source itself rather than the Galactic ridge.

We perform pulse phase resolved spectral analysis of the source using the first three *RXTE* observations. From this analysis, we find a marginal evidence of a variation of the photon index and the folding energy of the high-energy cut-off with the pulse phase (see Fig. 9).

ACKNOWLEDGEMENTS

We acknowledge support from TÜBİTAK, the Scientific and Technological Research Council of Turkey through the research project TBAG 109T748.

REFERENCES

Barthelmy S. D. et al., 2005, Space Sci. Rev., 120, 143
Baykal A., Ögelman H., 1993, A&A, 267, 119
Baykal A., İnam S. Ç., Stark M. J., Heffner C. M., Erkoca A. E., Swank J. H., 2007, MNRAS, 374, 1108
Bildsten L. et al., 1997, ApJS, 113, 367
Burrows D. N. et al., 2005, Space Sci. Rev., 120, 165
Corbet R. H. D., 1984, A&A, 141, 91
Cordes J. M., 1980, ApJ, 237, 216
Deeter J. E., 1984, ApJ, 281, 482
Deeter J. E., Boynton P. E., 1985, in Hayakawa S., Nagase F., eds, Proc. Inuyama Workshop: Timing Studies of X-Ray Sources. Nagoya Univ., Nagoya, p. 29
Deeter J. E., Boynton P. E., Pravdo S. H., 1981, ApJ, 247, 1003
Drave S. P., Bird A. J., Townsend L. J., Hill A. B., McBride V. A., Sguera V., Bazzano A., Clark D. J., 2012, A&A, 539, 21
Gehrels N. et al., 2004, ApJ, 611, 1005
Jahoda K., Swank J. H., Giles A. B., Stark M. J., Strohmayer T., Zhang W., Morgan E. H., 1996, in Siegmund O. H., Gummin M. A., eds, Proc. SPIE, Vol. 2808, EUV, X-Ray, and Gamma-Ray Instrumentation for Astronomy VII. SPIE, Bellingham, p. 59
Leahy D. A., Darbro W., Elsner R. F., Weisskopf M. C., Kahn S., Sutherland P. G., Grindlay J. E., 1983, ApJ, 266, 160
Leahy D. A., Matsuoka M., Kawai N., Makino F., 1989, MNRAS, 236, 603
Markwardt C. B., Krimm H. A., Swank J. H., 2010a, Astron. Telegram, 2747
Markwardt C. B., Krimm H. A., Swank J. H., 2010b, Astron. Telegram, 2749
Moretti A. et al., 2005, SPIE, 5898, 360
Ohashi T. et al., 1984, PASJ, 36, 699
Parmar A. N., White N. E., Stella L., 1989, ApJ, 338, 373
Paul B., Agrawal P. C., Rao A. R., Manchanda R. K., 1997, A&A, 319, 507
Reig P., Nespoli E., 2013, A&A, 551, A1
Valinia A., Marshall F. E., 1998, ApJ, 505, 134
Vaughan S. et al., 2006, ApJ, 638, 920

This paper has been typeset from a TEX/LATEX file prepared by the author.

Downloaded from https://academic.oup.com/mnras/article-abstract/434/4/2772/954751 by MIDDLE EAST TECHNICAL UNIVERSITY LIBRARY user on 24 July 2020